

# Supplemental Material for Topological phenomena in artificial quantum materials revealed by local Chern markers

Catalin D. Spataru,<sup>1,\*</sup> Wei Pan,<sup>1,†</sup> and Alexander Cerjan<sup>2,‡</sup>

<sup>1</sup>*Sandia National Laboratories, Livermore, California 94551, USA*

<sup>2</sup>*Center for Integrated Nanotechnologies, Sandia National Laboratories, Albuquerque, New Mexico 87185, USA*

## SI. Methods

### A. Experiment

Interferometric lithography (IL) is used to fabricate artificial graphene (AG). First, a square specimen of size 5 mm  $\times$  5 mm is cleaved from an as-grown AlSb/InAs/AlSb quantum well (QW) wafer. Then, a layer of photoresist of  $\sim 1.5 \mu\text{m}$  thick is spun on the specimen. To create the honeycomb structure needed for AG, interference of two coherent laser beams defines the first set of parallel lines. Then the specimen is rotated by  $60^\circ$  and the second set of parallel lines is defined. The crossing points of the two sets of lines then create a triangular holes array after photoresist develop. Subsequent reactive ion etching produces holes array in the 2D electron gas in the InAs QW. The unetched area forms a honeycomb lattice, leading to the formation of AG. An SEM (scanning-electron-microscope) image of a fabricated device, made using this procedure, is shown in Fig. 1b of the main text.

### B. Modeling

We used the lattice parameters  $\Delta x = \Delta y = 2 \text{ nm}$  which together with  $m_{\text{eff}} = 0.023$  (typical of the experimental sample) yields  $t^{(\text{FD})} \approx 414 \text{ meV}$ . This implies that the physics of the 2D electron gas is well described for  $E_F$  within 100 meV from the bottom of the electron band. When a magnetic field is present, the finite different description is also only valid so long as the magnetic length is larger than the grid spacing,  $l_B \gg \Delta x$ . The potential  $V(\mathbf{x})$  accounts for circular patterns via a muffin-tin on-site potential with strength  $V_h$  and triangular symmetry. The AG pseudo-atoms develop with a honeycomb symmetry in between the circles (see Fig. 1a of the main text).

A perpendicular magnetic field  $\vec{B} = B\hat{z}$  is introduced via the Peierls substitution within the Landau gauge  $\vec{A} = Bx\hat{y}$  where  $\vec{A}$  is the vector potential. In this gauge the hopping parameters  $t^{(\text{FD})}$  between neighboring lattice sites  $j, l$  take the form (for sites aligned along  $\hat{x}$  and  $\hat{y}$  respectively):  $t_{j,l}^{(x)} = t$  and  $t_{j,l}^{(y)} = te^{\pm 2\pi i n p / N_x}$  where  $N_x$  is the number of vertices along  $\hat{x}$ ,  $n\Delta_x$  is the  $j$ -vertex coordinate along  $\hat{x}$  and  $p$  is the magnetic flux per discretized ribbon (with area  $N_x\Delta x\Delta y$ ) in units of the magnetic flux quantum  $\Phi_0 = h/e$ . When periodic boundary conditions (PBC) are imposed,  $p$  takes an integer value and represents the magnetic flux through the magnetic supercell. In general the calculations assume that the spins are independent and degenerate. For the purpose of comparing to experiment the degeneracy is relaxed by assuming an effective Landé factor with a fitted value  $g = 40$ . In this case the eigenvalues of  $H^{(\text{FD})}$  are shifted by  $\mu_B g s_z B / \hbar$  where  $\mu_B$  is the Bohr magneton and  $s_z = \pm 1/2$  are the up/down components of the electron spin.

To parameterize our numerical model to our specific experimental system, we compare  $R_{xx}$  of the artificial graphene heterostructure against the density of states (DOS) of the discretized system [Figs. 1e,f in the main text]. In particular, we fit the positions of the lowest-filling Landau levels (measured for  $B > 3 \text{ T}$ ) with an analytic model for an unpatterned 2D electron gas and find excellent agreement for  $m^* = 0.023m_0$ , which yields a Fermi level  $E_F \equiv \pi n \hbar^2 / m^* \sim 85 \text{ meV}$ , and  $g = 40$ , where we are using a uniform Zeeman splitting approximation [1, 2]. The simulated energy levels are also broadened using a Lorentzian with full-width half-maximum 0.5 meV. In turn, these model parameters also yield quantitative agreement with the prominent Landau levels seen in  $R_{xx}$  of our artificial graphene heterostructure.

---

\* [cdspata@sandia.gov](mailto:cdspata@sandia.gov)

† [wpan@sandia.gov](mailto:wpan@sandia.gov)

‡ [awcerja@sandia.gov](mailto:awcerja@sandia.gov)

### C. Efficient determination of the local Chern marker

Numerically, the spectral localizer framework possesses two key features that lend it to efficient algorithms. First, it preserves sparsity, i.e., if  $X, Y, H$  are sparse, so is  $L_{(x,y,E)}$ . This is in contrast to other known local Chern markers that project into the occupied subspace [3, 4], which generally yields dense matrices. Second, the calculation of a matrix's signature does not require finding the matrix's spectrum, and can instead leverage results from applied mathematics such as Sylvester's law of inertia [5]. In particular, if  $NDN^\dagger$  is the LDLT decomposition of  $L_{(x,y,E)}$ , then  $\text{sig}[L_{(x,y,E)}] = \text{sig}[D]$ . Thus, as there are fast, sparse LDLT decomposition methods [6], the determination of  $C_{(x,y,E)}^L$  is generally orders of magnitude faster than the calculation of the spectrum of  $L_{(x,y,E)}$ , or finding the occupied subspace of  $H$  for the same system. Overall, as the spectral localizer is built from the  $K$ -theory of  $C^*$ -algebras and is compatible with a variety of numerical speedups, it is a numerical  $K$ -theoretic approach to material topology.

### SII. Analysis of states in between the Landau levels

In the discussion of Fig. 1 of the main text, we claim that the non-zero density of states (DOS) between the Landau levels seen in simulations is due to the presence of states pinned to the antidot potential elements, whose fine features in an ordered system [main text Fig. 2] are then blurred out by disorder. In this section, we provide further evidence for this claim. In Fig. S1a,b, we compare the DOS for simulations of ordered and disordered systems for both spin sectors, and find that the inclusion of disorder blurs out the fine features seen in the ordered system in Figs. 2a,b in the main text. In Fig. S1c-h, we both show the system potential and then reproduce Figs. 2c-g from the main text on a larger scale.

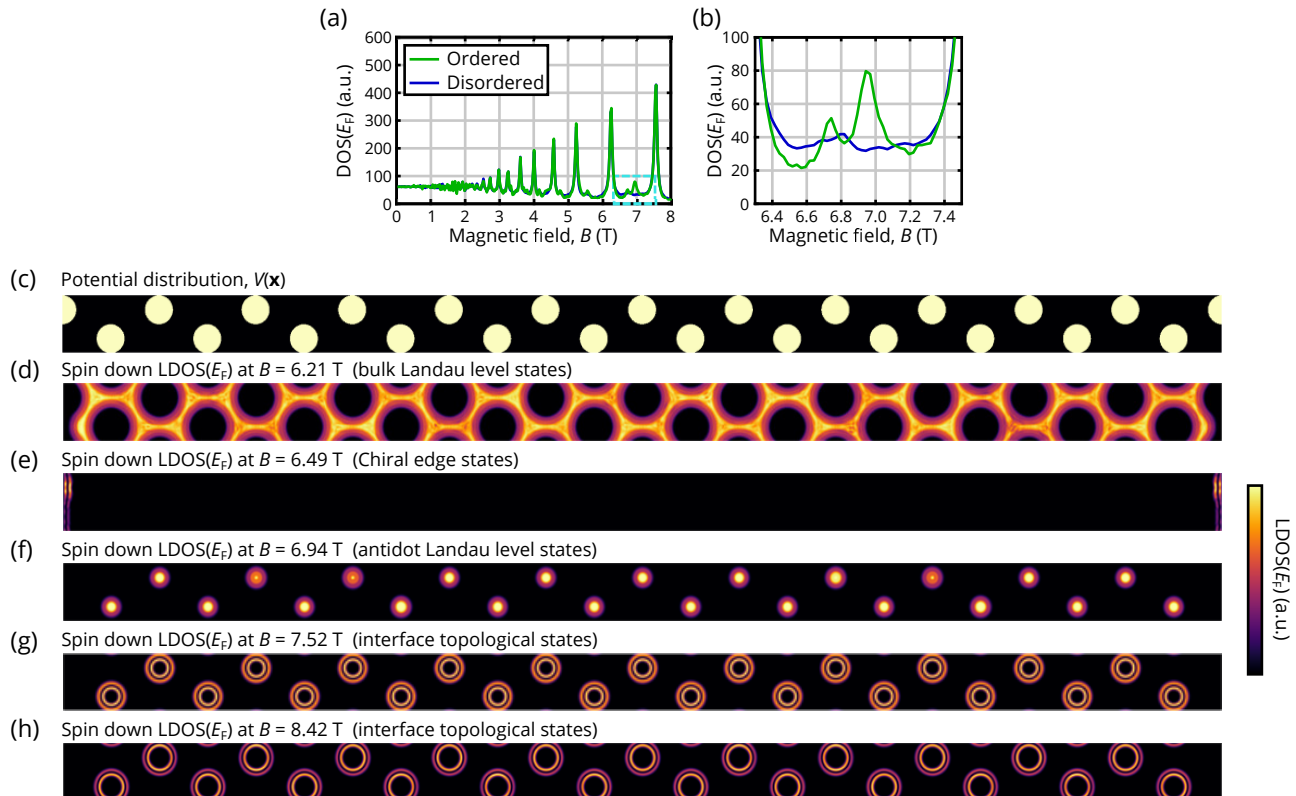


FIG. S1. (a) Density of states (DOS) at the Fermi energy for a given magnetic field strength for the same simulation model as is used in Fig. 1e,f of the main text. DOS for disordered (blue, same as main text) and ordered (green) with  $\delta V_h = 0$  meV systems are shown. In other words, the data for the ordered system is the combination of Figs. 2a,b in the main text. (b) Zoom-in of the  $\text{DOS}(E_F)$  in the dashed cyan box in (a). (c-g) Real space plots of the periodic electrostatic potential (c), as well as the local density of states (LDOS) at the Fermi energy for the same magnetic field strengths as considered in Figs. 2c-g from the main text.

### III. Verifying simulation convergence

In this section, we demonstrate that our simulated results shown in Fig. 1e of the main text are converged with respect to the spectral localizer's scaling coefficient  $\kappa$  as well as the size of the (simulated) finite flake. We also discuss the stability of the spectral localizer framework with respect to changes in  $\kappa$ .

#### A. Convergence with respect to the scaling coefficient $\kappa$

In the definition and discussion of the spectral localizer in Eq. (2) of the main text, it is noted that the function of the scaling coefficient  $\kappa$  is twofold, it ensures consistent units and it adjusts the relative weight between the position operators and Hamiltonian. This adjustment is necessary, as the two limits of  $\kappa$  each yield unhelpful spectral localizers. If  $\kappa = 0$  meV/nm, the spectral localizer is simply the block diagonal matrix  $(H - E\mathbf{1}) \otimes \sigma_z$ , whose signature is always zero as the two blocks have equal but opposite spectra. If  $\kappa \rightarrow \infty$  meV/nm, the spectral localizer simply contains information about the position operators, which commute, and thus  $\text{sig}[L_{(x,y,E)}] = 0$  as well. (Further discussion of these two limits of  $\kappa$  is provided in Sec. 4A of Ref. [7].) As such, the spectral localizer only provides a correct determination for material topology for a range of intermediate values of  $\kappa$  between these two limits, when the spectral weight between the Hamiltonian and position operators in  $L_{(x,y,E)}$  is relatively balanced.

For tight-binding models (or other models featuring bounded Hamiltonians) that describe single materials characterized by a single length scale, a range of validity for  $\kappa$  can be proven [8, Theorem 2]. However, one of these bounds depends on the  $\ell^2$  norm of the Hamiltonian; thus, for unbounded systems this bound on  $\kappa$  is not definable, as the  $\ell^2$  norm is not defined. It is not currently known how to adapt these proven bounds to the case of unbounded Hamiltonians. Nevertheless, in every case that we are aware of, the spectral localizer for unbounded systems still exhibits a range of  $\kappa$  over which the topological invariant is stable [9–11], generally near  $\kappa \sim E_{\text{gap}}/L_{\text{min}}$  as discussed in the main text. Indeed, Fig. S2 shows that the results in Fig. 1e of the main text can be quantitatively reproduced at larger magnetic fields for a range of  $\kappa$  spanning more than two orders of magnitude.

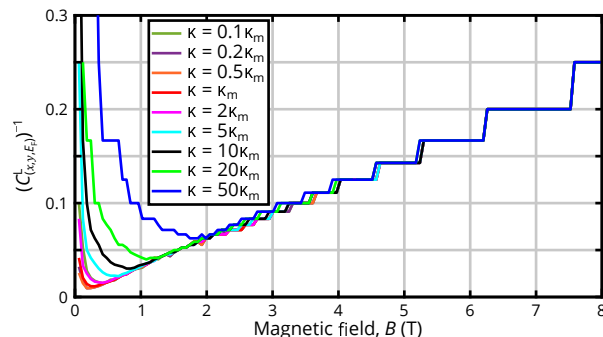


FIG. S2. Inverse of the local Chern marker at the Fermi energy versus magnetic field calculated for the same model parameters as Fig. 1e in the main text, using different values of  $\kappa$ . Here,  $\kappa_m = 1 \times 10^{-3}$  meV/nm is the value used in the main text.

In our simulations, we are usually choosing  $\kappa \sim E_{\text{gap}}/L_{\text{min}}$ , where  $L_{\text{min}}$  is the smallest dimension of the finite system and  $E_{\text{gap}} = \hbar\omega_c$  is the width of the relevant bulk spectral gap based on the cyclotron frequency at  $B = 7$  T. As such, it is expected that the local Chern number will show better convergence with respect to  $\kappa$  for larger magnetic fields, as discussed in the main text. We expect that the spectral localizer framework can accurately resolve the local Chern marker at smaller magnetic fields using a different  $\kappa$  and a larger simulation domain to increase  $L_{\text{min}}$ .

However, for multi-scale systems that can exhibit different properties at different length scales, changing  $\kappa$  enables the spectral localizer framework to be sensitive to the different topological phenomena at these different length scales. For example, while Fig. 1 in the main text analyzes the number of chiral edge states that appear at the boundaries of the sample, Fig. 2 studies the origins of the states pinned to each antidot that are dependent on the potential strength and diameter of the antidot and not the full sample. Thus, Fig. 1 uses  $\kappa \sim E_{\text{gap}}/L_{\text{min}}$ , while Fig. 2 uses the larger  $\kappa \sim 2E_{\text{gap}}/a$ , where  $a/2$  is the antidot diameter. Mathematically, the increased  $\kappa$  is placing greater emphasis on the position operators in  $L_{(x,y,E)}$ , so the signature is more responsive to changes in  $(x, y)$  and less responsive to changes in  $E$ , effectively limiting the function of the spectral localizer to larger magnetic fields where the local spectral gap is larger.

On its surface, the ability to change  $\kappa$  and obtain a different topological marker appears to present some confusion — for a given choice of  $(x, y, E)$ , what is the system's actual topology? For example, if  $(x, y)$  are chosen in the

center of an antidot of artificial graphene and  $E = E_F$ , the system appears to provide 3 different values for the local Chern marker. However, these different values are not actually in conflict, they simply reveal different physics on different length scales. For  $\kappa \sim E_{\text{gap}}/L_{\text{min}}$ , the local Chern marker is revealing sample-scale topology, and will correspond to the number of chiral edge states around the boundary of the full system. For  $\kappa \sim 2E_{\text{gap}}/a$ , the local Chern marker is showing antidot-scale topology, and predicts the number of antidot-bulk interface localized states. For  $\kappa \ll E_{\text{gap}}/L_{\text{min}}$ , the local Chern marker is 0, because there is no relevant physics at much larger length scales nor any material boundary or interface to support a boundary-localized state. Likewise, for  $\kappa \gg 2E_{\text{gap}}/a$ , the local Chern marker is again 0, again due to the lack of relevant phenomena at much shorter length scales.

In principle, the  $\kappa$  coefficient in front of  $(X - x\mathbf{1})$  and  $(Y - y\mathbf{1})$  could be different. However, as the scale of both position operators is set by the lattice constant  $a$ , choosing different  $\kappa$  adds unnecessary complexity for little benefit. If these two position operators were set by different system length scales, using different  $\kappa$  would likely be required.

## B. Stability of the spectral localizer framework's predictions with respect to $\kappa$

Broadly, the dependence of the spectral localizer framework on a scaling parameter such as  $\kappa$  is both expected, and can be viewed as a feature rather than a bug. First, to the best of our knowledge, all other frameworks for local topological markers have an equivalent choice of hyper-parameter. For example, both the Kitaev [3, Appendix C] and Bianco-Resta [4] markers require a choice of integration region(s) that must be sufficiently large so as to guarantee an approximately integer-valued local marker, but not so large as to contain any portion of a material's boundary (if a material's full boundary is contained, both of these local markers are provably 0). In the spectral localizer framework,  $\kappa$  is fulfilling a similar purpose as the choice of integration region in these other frameworks, with larger values of  $\kappa$  approximately corresponding to smaller integration regions that yield greater spatial specificity in the topological classification of a material at the cost of reduced spectral accuracy. Note, the spectral localizer's markers are always integer-valued regardless of the choice of  $\kappa$ .

Moreover, as discussed in Sec. III A, the ability to change  $\kappa$  allows the spectral localizer framework to both resolve sample-scale topology as well as internal regions within a sample that may have different local topology, but that do not contribute to a standard edge-conductance measurement (e.g., the different local topology of the antidots discussed in the main text in Fig. 2). But, how does one know when to trust that a calculated value of the local marker is revealing material phenomena rather than numerical noise? In this section, we detail how the spectral localizer framework comes inherently equipped with a measure of topological protection that can be heuristically viewed as a local spectral gap. This measure of robustness also includes protection against changes in  $\kappa$ . Thus, when this measure of protection is large, relative to the energy scales of the system, the spectral localizer's predictions correspond to real physical phenomena.

First, mathematically observe that changes in  $\kappa$  always change the spectrum of  $L_{(x,y,E)}$  continuously and thus the local marker  $C_{(x,y,E)}^L$  is necessarily stable against changes in  $\kappa$  so long as  $L_{(x,y,E)}$  remains invertible. In particular, so long as  $H$  is bounded,  $L_{(x,y,E)}$  is Hermitian and bounded, and as such its eigenvalues must move continuously with respect to perturbations to  $L_{(x,y,E)}$  at a rate limited by Weyl's inequality [12, 13]. For the specific case of perturbations in  $\kappa$ , if  $\kappa \rightarrow \kappa + \delta\kappa$ , then  $L_{(x,y,E)} \rightarrow L_{(x,y,E)} + \delta L_{(x,y,E)}$  with

$$\delta L_{(x,y,E)} = \delta\kappa(X - x\mathbf{1}) \otimes \sigma_x + \delta\kappa(Y - y\mathbf{1}) \otimes \sigma_y, \quad (\text{S1})$$

and thus if  $\lambda_j^{(\kappa)} \in \text{spec}[L_{(x,y,E)}]$  is the  $j$ th smallest eigenvalue of  $L_{(x,y,E)}$ , and  $\lambda_j^{(\kappa+\delta\kappa)} \in \text{spec}[L_{(x,y,E)} + \delta L_{(x,y,E)}]$  is similarly defined, then by Weyl's inequality

$$\left| \lambda_j^{(\kappa+\delta\kappa)} - \lambda_j^{(\kappa)} \right| \leq \|\delta L_{(x,y,E)}\|. \quad (\text{S2})$$

Here,  $\text{spec}[M]$  denotes the spectrum of  $M$ . Now, as the local Chern marker  $C_{(x,y,E)}^L$  defined in Eq. 3 of the main text is given by the difference in the number of positive eigenvalues minus the number of negative ones, the only way for  $C_{(x,y,E)}^L$  to change its value is if one of the spectral localizer's eigenvalues first becomes 0, i.e.,  $L_{(x,y,E)}$  becomes non-invertible. Altogether, this means that the spectral localizer framework is inherently equipped with a quantitative measure of topological protection

$$\mu_{(x,y,E)}(X, Y, H) = \min \left( \left| \text{spec} [L_{(x,y,E)}(X, Y, H)] \right| \right), \quad (\text{S3})$$

in other words, the smallest distance an eigenvalue of the spectral localizer must move before the system's local topological marker can change. Any perturbation to the spectral localizer with  $\|\delta L_{(x,y,E)}\| < \mu_{(x,y,E)}$  cannot change

the local Chern marker. This eigenvalue movement could be due to a chance in choice of  $(x, y, E)$ , a perturbation to the physical system  $H \rightarrow H + \delta H$ , or a change in  $\kappa$  as discussed. An example of this measure of topological protection is shown in Fig. S3, where  $\mu_{(x,y,E)}$  is plotted for changes in energy corresponding to the unconventional Landau levels discussed in Fig. 4 of the main text. As can be seen, the system's topological marker can only change across regions where  $\mu_{(x,y,E)} \rightarrow 0$ . (Note, the lack of exact zeros in Fig. S3 is simply due to the numerical sampling not perfectly aligning with the energies where these closings actually occur.)

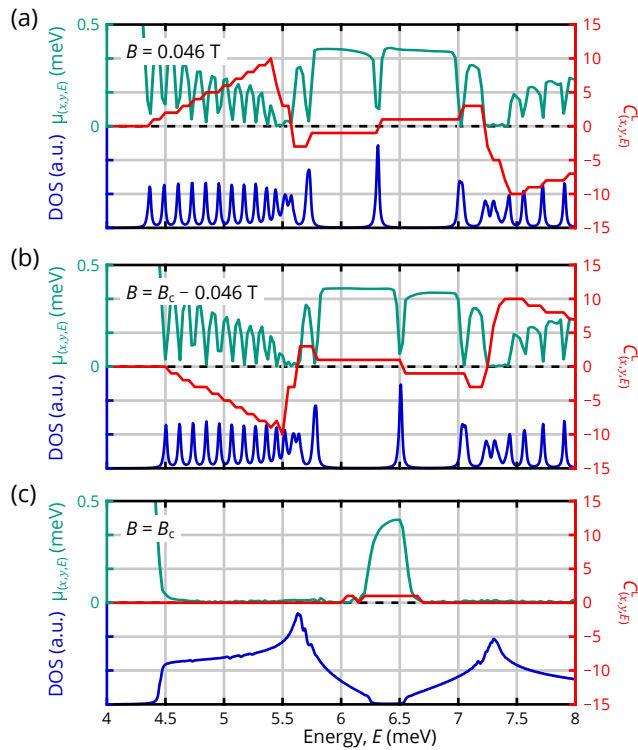


FIG. S3. (a-c) Local gap  $\mu_{(x,y,E)}$  (green), density of states (blue) and  $C^L_{(x,y,E)}$  in the unpatterned bulk (red) for a single spin sector of artificial graphene with  $V_h \rightarrow \infty$  meV using the same simulation parameters as Fig. 3 in the main text for magnetic field strengths near  $B \sim 0$  T and the critical field  $B \sim B_c$  where  $\Phi = \Phi_0$ .

Altogether, the predictions of the spectral localizer framework for a given  $\kappa$  can be trusted when the local gap  $\mu_{(x,y,E)}$  is similar to or larger than the relevant energy scale of the system. (Note that by definition  $\mu_{(x,y,E)}$  has units of energy.) In practice, one generally wants to coarsely sweep  $\kappa$  over a few orders of magnitude in the vicinity of  $\kappa \sim E_{\text{gap}}/L_{\text{min}}$  for choices of  $(x, y, E)$  where one suspects a system might be topological and choices of  $L_{\text{min}}$  corresponding to a system's relevant length scales. While this sweep may miss small  $\kappa$  intervals where the system has a non-trivial local marker, by Eqs. (S2) and (S3) the robustness of any associated topological phenomena will necessarily be weak. This weakness could manifest as either an associated edge state being sensitive to system perturbations, or a difficulty in even identifying an associated edge state(s) in the system's LDOS as the state is delocalized; small values of  $\mu_{(x,y,E)}$  correspond to locations where the system has an approximate state [14] so large regions where  $\mu_{(x,y,E)} \approx 0$  typically indicate regions with one or many delocalized states (e.g., as can be seen via comparison of  $\mu_{(x,y,E)}$  with the DOS in Fig. S3).

Before concluding this section, we note that recent mathematical results show that the entire operation of the spectral localizer framework for classifying 1D systems can be understood through the response of the spectrum of  $L_{(x,y,E)}$  to changes in  $\kappa$  [15], demonstrating that  $\kappa$  may be even more integral to the spectral localizer framework than previously appreciated.

### C. Convergence with respect to simulation domain size

As the spectral localizer must be used in conjunction with a finite system, here we confirm that the results shown in Fig. 1e for the local Chern marker are converged with respect to the choice of simulated system size. In Fig. S4 we show calculations using three different system sizes that are nearly identical, especially in the high-field limit, despite

featuring very different system sizes.

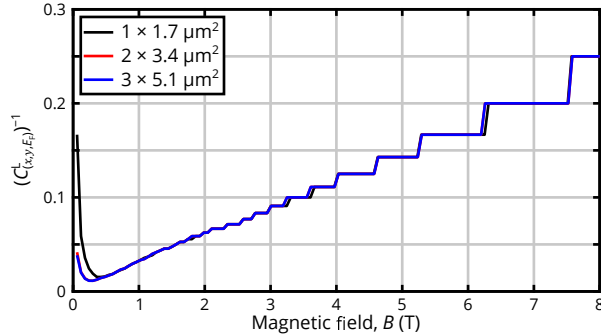


FIG. S4. Inverse of the local Chern marker at the Fermi energy versus magnetic field calculated for the same model parameters as Fig. 1e in the main text, using different simulation domains  $\sim 1 \times 1.7 \mu\text{m}^2$ ,  $\sim 2 \times 3.4 \mu\text{m}^2$  (same as main text), and  $\sim 3 \times 5.1 \mu\text{m}^2$ .

#### SIV. Band structures for the emergence of Hofstadter’s butterfly

In Fig. 3 of the main text, we show the emergence of Hofstadter’s butterfly as the strength of the periodic potential is increased from zero. In Fig. S5, we show the corresponding bulk band structures at  $B = 0$  T to show the energy of the Dirac point as well as the energy of the bottom of the bands.

#### SV. Hofstadter’s butterfly at larger scales

Compared to natural graphene, artificial graphene offers broad versatility as its properties can be modified by adjusting the parameters of the nanoscale antidot pattern, such as the lattice constant and antidot potential strength. However, in contrast to natural graphene, probing the energy range near the Dirac point can be challenging in artificial graphene, as achieving  $E_F \sim E_D$  requires reaching electron densities on the order of  $n \sim 10^{10} \text{ cm}^{-2}$  for typical lattice periodicities of 100 nm. Nevertheless, the spectral localizer reveals that it is possible to observe Hofstadter phenomena, such as the rapid sign change of the Chern marker across lines where  $\Phi/\Phi_0 \in \mathbb{Z}$  and potentially even full butterflies, for  $E_F \gg E_D$  in artificial graphene [Fig. S6]. Here, the Chern marker fringes seen for stronger  $B$  are likely a finite size effect, and can be qualitatively reproduced in tight-binding simulations of a honeycomb lattice [see Sec. SV A]. Thus, so long as an experimental system can realize a sufficiently strong antidot potential  $V_h > E_F$ , the spectral localizer predicts that Hofstadter phenomena should manifest for larger electron densities that are easier to obtain in experiments; for example, rapid changes in the Chern marker appear in Fig. S6 for  $E_F = 35 \text{ meV}$ , which corresponds to  $n \sim 4.4 \times 10^{11} \text{ cm}^{-2}$ .

##### A. Local Chern marker fringes in tight binding models

In Fig. S6, simulations of the local Chern marker for artificial graphene, fringes are seen for larger energies and magnetic field strengths. In this section, we demonstrate that these fringes are consistent with finite size effects seen in calculations of the local Chern marker in a tight-binding lattice. Specifically, we consider a tight-binding honeycomb lattice with only nearest neighbor couplings [16], and calculate its local Chern marker using the spectral localizer for two different choices of finite flakes. As can be seen in Fig. S7, for small simulation domains, fringes appear in some of the butterfly’s minigaps that should show a single value for the local Chern marker. As the simulation domain is increased in size, these fringes disappear. Additionally, the larger simulation domain enables the resolution of local Chern markers with larger magnitudes. This latter behavior is consistent with the difference seen between Fig. 1c and Fig. 1e of the main text between the local Chern marker and measured Hall conductivity at low magnetic field strengths; resolving larger Chern marker magnitudes requires ensuring the system is large enough so that the corresponding edge-localized states do not couple to states from the opposite edge, rendering the states trivial. Similarly, we suspect that the fringes in regions with small-magnitude local Chern markers originate from the angular quantization of the chiral edge states due to the simulated system’s finite size—the smaller the system

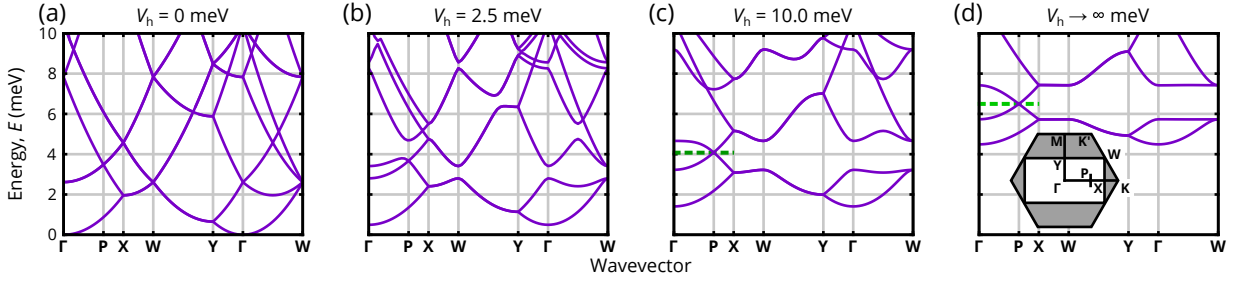


FIG. S5. (a-d) Artificial graphene's bulk band structures at  $B = 0$  T for  $V_h = 0$  meV (a) to 2.5 meV (b), 10 meV (c), and finally  $\infty$  meV (d). The lowest energy Dirac point is marked in the systems with spectrally isolated Dirac points (green dashed lines), and this energy is indicated in the corresponding Chern marker plots (green arrows) in Fig. 3 of the main text.

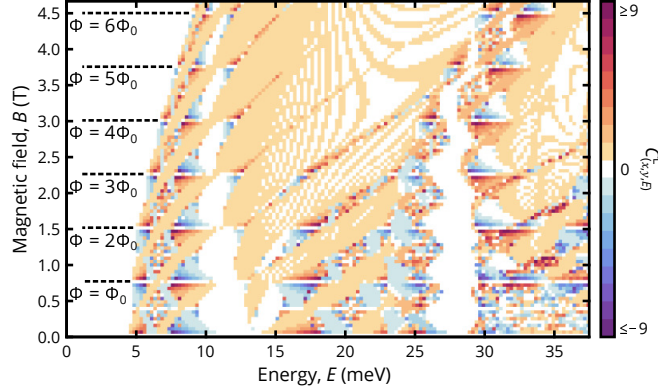


FIG. S6. Predicted local Chern marker  $C_{(x,y),E}^L$  in the unpatterned bulk for a single spin sector as a function of magnetic field strength and energy for the same ordered artificial graphene system considered in Fig. 3 of the main text with  $V_h \rightarrow \infty$  meV.

area, and thus the smaller the system boundary, the larger the spectral spacing between the edge states, potentially providing an opportunity for the spectral localizer to misclassify the system's topology within these spectral gaps. Altogether, we suspect that the fringes seen in Fig. S6 of the main text could also be returned to a single Chern marker by increasing the simulation domain of the artificial graphene used.

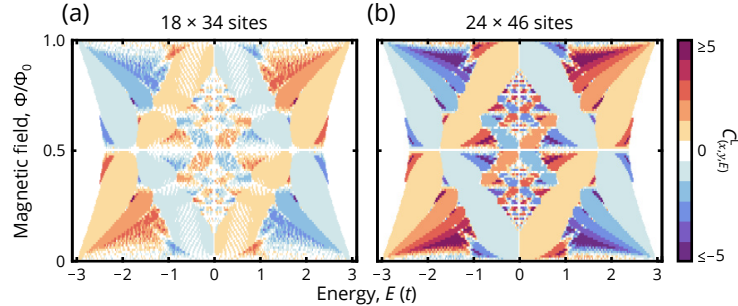


FIG. S7. Local Chern marker  $C_{(x,y),E}^L$  in the unpatterned bulk as a function of energy and magnetic field strength in normalized units for a tight-binding honeycomb lattice with  $18 \times 34$  (a) or  $24 \times 46$  (b) sites. Simulations use  $\kappa = 0.007(t/a)$  where  $t$  is the nearest neighbor coupling strength and  $a$  is the lattice constant.

## SVI. Extended data for the unconventional quantum Hall effect in artificial graphene

In Fig. 4 of the main text, we discuss the appearance of the unconventional quantum Hall effect in artificial graphene near both  $B = 0$  T and  $B = B_c$ . In Fig. S8a-f, we show additional data to help verify both the square root dependence of the Landau level gaps as well as the change in Chern number by 2 per spin sector. Moreover, we also compare

the ribbon band structures (i.e., the band structures of systems that are periodic in one direction and open in the other) of the continuum models at  $B = 0\text{T}$  and  $B = B_c$ , as well as a tight-binding model with nearest neighbor (NN) and next-nearest neighbor (NNN) couplings  $t_{\text{NNN}}/t_{\text{NN}} = 0.13$ . First, by comparing Fig. S8g and Fig. S8h, we conclude that artificial graphene has next-nearest neighbor couplings between its pseudo-atoms that are  $\sim 13\%$  of the strength of the couplings between the nearest neighbor pseudo-atoms, but also that there are additional longer-range couplings beyond NNN couplings in artificial graphene, as the agreement is not perfect. We note that the difference between the edge states along the direction with open boundaries is due to artificial graphene having a half-potential at its edge [see Fig. S1c] that is known to change the dispersion of the edge states [17]. Similarly, comparing Fig. S8g and Fig. S8i shows the opening of a bulk band gap crossed by a pair of chiral edge states, confirming that artificial graphene becomes a topological insulator at  $B = B_c$ .

- 
- [1] S. S. Krishtopenko, V. I. Gavrilenko, and M. Goiran, Theory of g-factor enhancement in narrow-gap quantum well heterostructures, *J. Phys.: Condens. Matter* **23**, 385601 (2011).
  - [2] W. Pan, K. W. Baldwin, K. W. West, L. N. Pfeiffer, and D. C. Tsui, Quantitative examination of the collapse of spin splitting in the quantum Hall regime, *Phys. Rev. B* **84**, 161307 (2011).
  - [3] A. Kitaev, Anyons in an exactly solved model and beyond, *Ann. Physics* **321**, 2 (2006).
  - [4] R. Bianco and R. Resta, Mapping topological order in coordinate space, *Phys. Rev. B* **84**, 241106 (2011).
  - [5] J. Sylvester, XIX. A demonstration of the theorem that every homogeneous quadratic polynomial is reducible by real orthogonal substitutions to the form of a sum of positive and negative squares, *The London, Edinburgh, and Dublin Philosophical Magazine and Journal of Science* **4**, 138 (1852).
  - [6] I. S. Duff, MA57—a code for the solution of sparse symmetric definite and indefinite systems, *ACM Trans. Math. Softw.* **30**, 118 (2004).
  - [7] A. Cerjan and T. A. Loring, Classifying photonic topology using the spectral localizer and numerical K-theory, *APL Photonics* **9**, 111102 (2024).
  - [8] T. A. Loring and H. Schulz-Baldes, The spectral localizer for even index pairings, *J. Noncommut. Geom.* **14**, 1 (2020).
  - [9] A. Cerjan and T. A. Loring, An operator-based approach to topological photonics, *Nanophotonics* **11**, 4765 (2022).
  - [10] K. Y. Dixon, T. A. Loring, and A. Cerjan, Classifying Topology in Photonic Heterostructures with Gapless Environments, *Phys. Rev. Lett.* **131**, 213801 (2023).
  - [11] A. Cerjan, T. A. Loring, and H. Schulz-Baldes, Local markers for crystalline topology, *Phys. Rev. Lett.* **132**, 073803 (2024).
  - [12] H. Weyl, Das asymptotische Verteilungsgesetz der Eigenwerte linearer partieller Differentialgleichungen (mit einer Anwendung auf die Theorie der Hohlraumstrahlung), *Math. Ann.* **71**, 441 (1912).
  - [13] R. Bhatia, *Matrix Analysis*, Graduate Texts in Mathematics, Vol. 169 (Springer New York, New York, NY, 1997).
  - [14] A. Cerjan, T. A. Loring, and F. Vides, Quadratic pseudospectrum for identifying localized states, *J. Math. Phys.* **64**, 023501 (2023).
  - [15] J. Shapiro, The Loring–Schulz-Baldes Spectral Localizer Revisited (American Mathematical Society, 2025).
  - [16] A. Agazzi, J.-P. Eckmann, and G. M. Graf, The Colored Hofstadter Butterfly for the Honeycomb Lattice, *J. Stat. Phys.* **156**, 417 (2014).
  - [17] W. Yao, S. A. Yang, and Q. Niu, Edge States in Graphene: From Gapped Flat-Band to Gapless Chiral Modes, *Phys. Rev. Lett.* **102**, 096801 (2009).

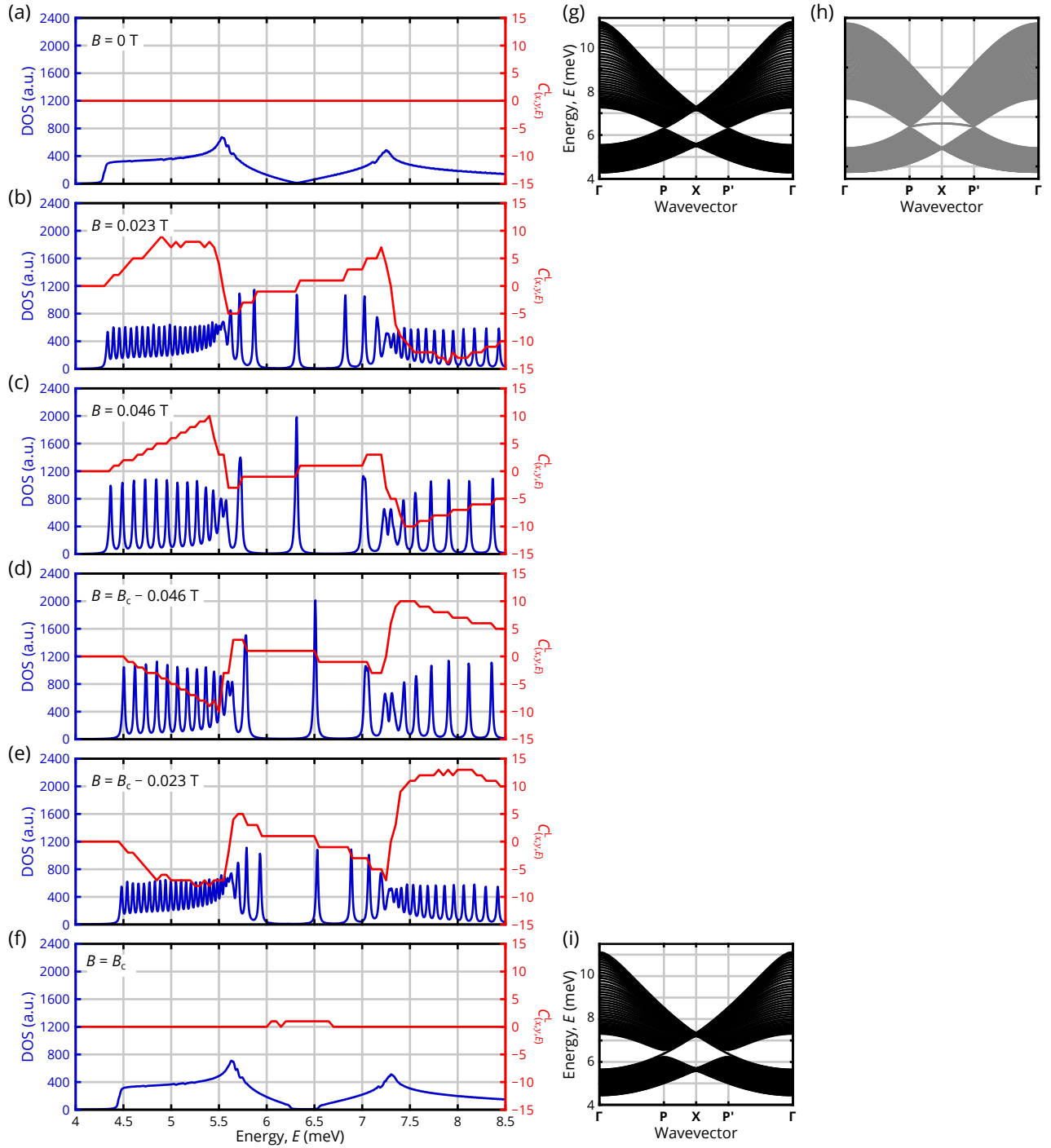


FIG. S8. (a-f) Density of states (blue) and  $C_{(x,y),E}^L$  in the unpatterned bulk (red) for a single spin sector of artificial graphene with  $V_h \rightarrow \infty$  meV using the same simulation parameters as Fig. 3 in the main text for magnetic field strengths near  $B \sim 0$  T and the critical field  $B \sim B_c$  where  $\Phi = \Phi_0$ . Some panels show the same data as Fig. 4 in the main text, except using a uniform DOS axis to allow for direct comparison. (g-i) Ribbon band structures along the remaining wavevector with open boundary conditions in the other direction for the continuum model at  $B = 0$  T (g), a honeycomb tight-binding lattice with  $t_{NNN}/t_{NN} = 0.13$  (h), and the continuum model at  $B = B_c$  with a convenient choice of gauge for the vector potential (i).